Data Repository Material

Table DR1. Station Locations, Data Yields and Splitting Measurements and Averages

Station	Lat.	Lon.	RFs	ϕ		δt		
	°	°		°	±	s	±	mean
MLOS+PATM	14.9226	-24.381	26	-66.0	2.0	1.40	0.10	
SACV	14.9702	-23.608	54	-77.0	6.0	0.55	0.15	
SACV+MAIO	15.2306	-23.177		-75.0	22.5	0.24	0.13	
MAIO	15.2306	-23.177	20					
SALA	16.7328	-22.936	23	-54.0	4.0	0.68	0.10	
S&E δt mean								0.82
SNIC	16.6201	-24.346	11	-8.0	22.5	2.20	1.10	
MING+PJOR	16.9235	-25.065		-13.0	8.0	0.72	0.25	
MING	16.8628	-24.936	22					
PJOR	16.9841	-25.194	12					
N δt mean								0.79
all island δt mean								0.81

Number of RFs used for each island in the average azimuthal stack. MLOS and PATM are two stations on the island of Fogo separated by $\sim$5 km, thus the number of RFs used for Fogo is the sum of MLOS and PATM. ϕ is the fast polarization direction, azimuth in degrees. δt is the delay time, in seconds. 1-σ uncertainties reported. SACV+MAIO indicates results for SACV and MAIO combined to yield joint estimate due to their proximity; similar for MING+PJOR.

Means calculated with weights $1/\sigma^2$.

Forward modeling example: Santiago (SACV)

Although there are 54 events in the average azimuthal stack for Santiago, due to poor back azimuthal coverage (Fig. DR1), the modeling considers only homogeneous, isotropic, flat lying layers. The velocity-depth modeling has two stages: 1) the initial forward modeling to determine a velocity-depth structure that produces a synthetic RF that matches the data within observational uncertainty ($\pm$2 standard deviations), and 2) the grid search, that uses the velocity-depth model found in stage (1) as the starting model to produce a range of acceptable velocity-depth models for a particular station. The SACV data exhibits several prominent features (Fig. 2), that may be selected for potential modeling. Initially, a simple 2-layer velocity-depth model is used, with the number of layers increased until all the observed peaks and troughs are modelled (Fig. DR2, Parts A-D show the forward modeling steps for Santiago island (SACV), as the number of layers are increased). The direct P arrival at 0 s has a shoulder which may be modelled with a 2-layer velocity-depth model that produces a P-to-S conversion at $\sim$1.2 s. A P-to-S conversion at this time produces multiples that correspond to the peaks at $\sim$4.5 s and $\sim$5.5 s (figure DR2 (A) and table DR2).

Table DR2. Two-layer velocity-depth model for Santiago

layer number	v_p (km s^{-1})	v_s (km s^{-1})	ρ (g cm^{-3})	thickness (km)	Poisson's ratio
1	6.0000	3.4286	2.8754	10.100	0.25
2	6.8400	3.8889	3.0306	∞	0.25

Although this 2-layer model matches the amplitudes of both the Ps and the multiple arrivals, it provides no explanation for the presence of the positive peak at $\sim$2.2 s. To model this arrival as a

P-to-S conversion requires the introduction of a deeper layer with a velocity increase across this new boundary because it is a positive peak. With a 3-layer model, not only can this arrival be modelled, but it produces multiples that approximately correspond to the positive and negative arrival at ∼7.5 s and ∼9.5 s respectively (figure DR2 (B) and table DR3).

Table DR3. Three-layer velocity-depth model for Santiago

layer number	v_p (km s^{-1})	v_s (km s^{-1})	ρ (g cm^{-3})	thickness (km)	Poisson's ratio
1	6.0000	3.4286	2.8754	10.100	0.25
2	6.8400	3.8889	3.0306	8.000	0.25
3	8.1000	4.6286	3.2689	∞	0.25

This 3-layer model clearly reproduces the timing of arrivals well, but unlike the 2-layer case, only the amplitude of the Ps arrival is matched. Further modeling shows that whilst the P-to-S conversion amplitude is more strongly controlled by the velocity contrast across the boundary, the multiple amplitude is more strongly controlled by the impedance contrast. Thus if the Ps amplitude is matched but the multiples amplitude is too large, then to reduce their amplitude, the density of the layer must be reduced. The important distinction to understand is that the velocity contrast controls both the timing and amplitude of the Ps arrival and its associated multiples, whereas the density contrast controls the amplitude of the arrivals only, with a very minor effect on the Ps amplitude and a much greater effect on the associated multiples amplitude. Therefore, as the amplitude and timing of the Ps arrival for this boundary are well matched, but the multiple amplitude is not, to maintain the fit to the Ps, only density may be varied. For SACV, the amplitude of the multiples may be better modelled by reducing the density in layer

3, from 3.27 g cm^{-3} to 2.7 g cm^{-3}, whilst all other parameters are held constant (figure DR2 part (C)). This leaves only the prominent negative arrival at around 9 s to be modelled. In RF analysis, a velocity inversion across a boundary produces a negative Ps arrival. If we introduce a velocity decrease from layer 3 into a layer 4, then the synthetic RF matches the data well (figure DR2 (D), table DR4). This four layer velocity-depth model is used as the starting model for the grid search.

Table DR4. Four-layer velocity-depth model for Santiago

layer number	v_p(km s^{-1})	v_s (km s^{-1})	ρ (g cm^{-3})	thickness (km)	Poisson's ratio
1	6.0000	3.4286	2.8754	10.100	0.25
2	6.8400	3.8889	3.0306	8.000	0.25
3	8.1000	4.6286	3.2689	70.000	0.25
4	7.4700	4.2425	3.1497	∞	0.25

The input parameters used for the gridsearch for the Santiago data are as follows:

- v_p/v_s ratio values from 1.65-1.85 in 0.05 increments (this corresponds to a range of Poisson's ratio from $\sim$0.21-$\sim$0.29).
- layer 1 v_p starting values from 5.0-6.6 km s^{-1} in 0.4 km s^{-1} increments

As the forward modeling indicates a 4-layer case, there are three P-to-S conversion arrival times, Ps_1, Ps_2 and Ps_3 from boundary 1, 2 and 3 respectively. To calculate the thickness of each layer given the velocities in that layer, requires δt

- Layer 1: $\delta t_1 = Ps_1$ = 1.26

- Layer 2: $\delta t_2 = Ps_2 - Ps_1$ = 0.89
- Layer 3: $\delta t_3 = Ps_3 - Ps_2$ = 6.48

The v_s ratios across each boundary, which produce the correct amplitudes for the data are as follows:

- Layer 1: Layer 2 = 1.12
- Layer 2: Layer 3 = 1.19
- Layer 3:Layer 4 = 0.92

The density(ρ) values in g cm^{-3} for the crustal densities are calculated (Christensen and Salisbury, 1975):

- ρ_1 = $(v_{s1} * 0.337) + 1.72$
- ρ_2 = $(v_{s2} * 0.337) + 1.72$

As discussed in the forward modeling, the density in layer 3 needs to be lower than expected given its velocity. Three different relationships are used to calculate the density in this layer. The first uses the ratio of the impedance contrast across the boundary between layers 2 and 3 which produces multiples that match the data well. The second uses a higher value for the impedance contrast ratio, thus increasing the amplitude of the multiples, but not as much as the third which uses a standard velocity-density relationship for mantle densities (Birch, 1961):

- $\rho_3 = (v_{s2} * \rho_2 * 1.06)/v_{s3}$

- $\rho_3 = (v_{s2} * \rho_2 * 1.16)/v_{s3}$
- $\rho_3 = (v_{p3} + 1.87)/3.05$

Finally, the density of layer 4 is calculated using (Birch, 1961):

- $\rho_4 = (v_{p4} + 1.87)/3.05$

Initially, the gridsearch produces 9375 models, which show a range of velocities and depths. However, any models with a $v_p > 9$ km s^{-1} are excluded, as these velocities are not physically viable in the depths being considered here (Gudmundsson and Sambridge, 1998). The velocity-depth models are used to produce synthetic receiver functions for comparison with the data. Chi-squared values are calculated:

$$\chi^2 = \sum_{i=1}^{N} \left(\frac{d(i) - s(i)}{\sigma(i)} \right)^2 \quad (1)$$

where d(i) are the data values, s(i) are the synthetic values and σ(i) are the standard deviation values (Fig. DR2 and Fig. DR3 show the $\pm 2\sigma$ bounds for all the stations). When d(i)=s(i), $\chi^2 = 0$ and therefore the lowest value gives the best fitting synthetic (Fig. 2). The range of acceptable models is found using a significance level of 0.05 (95% confidence interval). For Santiago, there are 317 acceptable models, the mean best fitting model is shown in Table DR5.

Table DR5. Best-fitting four-layer velocity-depth model for Santiago

layer number	v_p(km s^{-1})	v_s (km s^{-1})	ρ (g cm^{-3})	thickness (km)	Poisson's ratio
1	6.2000	3.5429	2.9139	10.436	0.2576
2	7.4342	4.0185	3.0742	7.763	0.2936
3	8.8483	4.7828	2.7379	67.469	0.2936
4	7.2334	4.3839	2.9847	∞	0.2097

The densities derived in this methodology are biased to low values because the inter layer v_s ratios in layers 1-3 are fixed to force the synthetic RFs to match the corresponding Ps amplitudes in the data. The densities derived from the density-velocity relation in each layer do not reflect the uncertainty in the Ps amplitudes. However, by calculating the melt fractions for higher densities as shown below, we show that this does not affect our argument relating the density to swell features.

The poor back azimuthal coverage (Fig. DR1) rules out investigating models that include anisotropy or dipping layers to explain the low amplitudes of the multiples from the top of the subcrustal layer. Thus gradational boundaries were investigated as an alternative to lowering the density. However, although a gradational boundary at the top of the subcrustal layer reduces the amplitude of the multiples from this boundary, due to the prominent Ps arrival from it, no gradational boundary models could match the amplitude and shape of the Ps arrival. Modeling showed that to maintain a good fit to the Ps arrival, models could not include a steep gradient and to match the multiples, even gradational boundary models required a density decrease, although not as significant as for the sharp boundaries used throughout this study. Thus the density value found here is an absolute minimum, given the assumptions of homogenous, isotropic, flat lying

layers with sharp impedance contrasts.

The key part of the argument is whether the subcrustal layer is fast or slow. Fast wavespeeds are required by the high amplitude of the Ps conversion at ∼2 s in all traces which is controlled by the velocity contrast at the top of the subcrustal layer. Numerical experiments show this feature to be insensitive to the layer density. Therefore the layer must be fast.

Temporary Network Results

The temporary network stations were modelled using the method described above and the best fitting synthetic RFs, along with the range of velocity-depth models that match the data for each island, are shown in Figure DR3.

Melt fractions calculated for higher densities

If the calculations for the mass of the swell root are repeated using a density upper bound of 3300 $\mathrm{kg\ m^{-3}}$ (Dziewonski and Anderson, 1981) for both the area of the whole swell and the area of the islands, then the edifice and crustal thickening represent a ∼1.0 wt% or ∼1.2 vol% and a ∼6.9 wt% or ∼8.3 vol% melt respectively. Therefore, although the density found with the RF analysis is anomalously low (due to the assumption of perfect elasticity, no shallow structural complexity and neglect of Ps amplitude uncertainty in fixing inter-layer velocity ratios), it produces melt fraction values similar to those for more reasonable mantle density values. The 8 m geoid anomaly reported in Cape Verde (Crough, 1982) would prescribe a density reduction of 88.6 $\mathrm{kg\ m^{-3}}$ through a layer thickness of 65 km (calculated from 80 km depth to the low-velocity

layer and subtracting a crustal thickness of 15 km; Turcotte and Schubert (2002)). This is within the density anomaly range yielding allowable OIB melting fractions.

References

Birch, F., 1961. The velocity of compressional waves in rocks to 10 kilobars, part 2. Journal of Geophysical Research 66, 2199–2224.

Christensen, N. I., Salisbury, M., 1975. Structure and constitution of the lower oceanic crust. Reviews of Geophysics 13, 57–86.

Crough, S. T., 1982. Geoid height anomalies over the Cape Verde Rise. Marine Geophysical Researches 5, 263–271.

Dziewonski, A. M., Anderson, D. L., 1981. Preliminary reference Earth model. Physics of the Earth and Planetary Interiors 25, 297–356.

Gudmundsson, O., Sambridge, M., 1998. A regionalized upper mantle (RUM) seismic model. Journal of Geophysical Research 103, 7121–7136.

Kennett, B. L. N., Engdahl, E. R., Buland, R., 1995. Constraints on seismic velocities in the Earth from traveltimes. Geophysical Journal International 122, 108–124.

Montagner, J.-P., Kennett, B. L. N., 1996. How to reconcile body-wave and normal-mode reference earth models. Geophysical Journal International 125, 229–248.

Turcotte, D. L., Schubert, G., 2002. Geodynamics. Cambridge University Press, Cambridge.

Figure DR1. Azimuthal equidistant plot centred on Santiago (SACV). Red circles indicate usable earthquake locations for the RF analysis. Range circles spaced every 30 degrees distance. Northern, southern and south-eastern back-azimuths are poorly represented in the dataset.

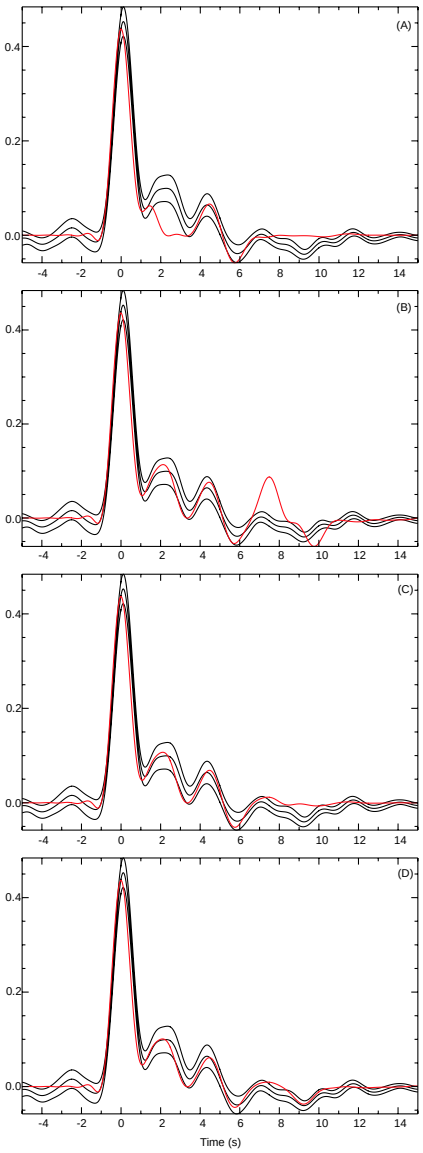

Figure DR2. Forward modeling steps for Santiago island (SACV). Black lines are the data and $\pm 2\sigma$ bounds and the red line is the best fitting synthetic RF. (A) Best fitting synthetic RF for a 2-layer model. (B) Best fitting synthetic RF for a 3-layer model. (C) As (B) but with a density decrease in layer 3. (D) Best fitting synthetic RF for a 4-layer model.

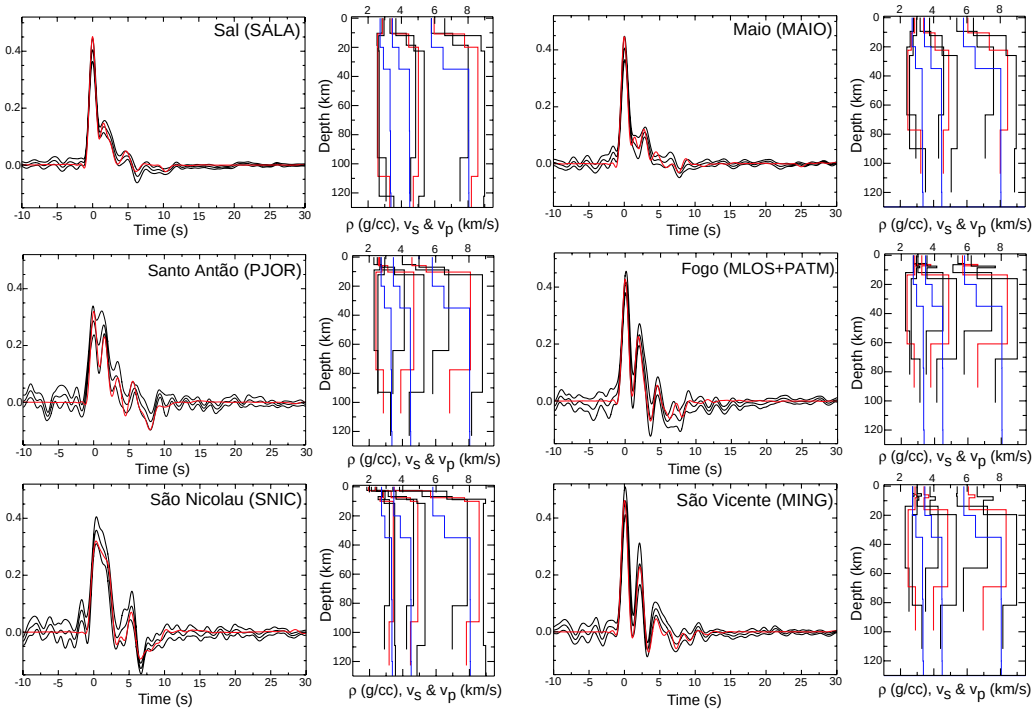

Figure DR3. Modeling of the RFs for the crustal and upper mantle structure beneath the temporary network stations (island and station names shown in figure). Left panels show the data $\pm 2\sigma$ in black lines, with the best fitting synthetic RF in red. The data is the average azimuthal stack of all events for a particular station. Right panels show the range of models produced with the grid search that give synthetic RFs that match the data to a prescribed level (within $\Delta\chi^2$). The red line is the mean model, the black lines are the maximum and minimum and the blue line is ak135 (Kennett et al., 1995, Montagner and Kennett, 1996) for reference. ρ is density, v_s is S-wave velocity and v_p is P-wave velocity.